Flux Linkage Tracking-Based Permanent Magnet Temperature Hybrid Modeling and Estimation for PMSMs With Data-Driven-Based Core Loss Compensation

Kaide Huang, Beichen Ding, *Member, IEEE*, Chunyan Lai, *Senior Member, IEEE*, and Guodong Feng, *Senior Member, IEEE*

***Abstract*—For permanent magnet synchronous machine (PMSM) drive, accurate magnet temperature is critical. The popular model-based magnet temperature estimation can be affected by core loss effect especially in the high-speed conditions. This article proposes a novel hybrid approach for accurate magnet temperature modeling and estimation, in which the estimation model is established by tracking the flux linkage variation, while the data-driven-based model is proposed to compensate the core loss effect. Specifically, the flux linkages in the rotating frame are projected into a new frame to derive the estimation model establishing the relationship between flux linkage variation and magnet temperature, in which the inverter distortion effect is canceled to improve the model accuracy. Based on this estimation model, the core loss effect is modeled, which indicates that the core loss influence is highly nonlinear and dependent on operating conditions. Hence, a radial basis function-based network is employed to model and compensate the core loss effect, and the network training is derived from the proposed model. The proposed hybrid approach can effectively improve the estimation performance especially at the high-speed conditions. Extensive experiments and comparisons are conducted on a laboratory interior PMSM drive to evaluate the proposed approach under various operating conditions.**

***Index Terms*—Core loss compensation, data-driven-based model, flux linkage variation, magnet temperature estimation, permanent magnet synchronous machine (PMSM).**

Manuscript received 17 April 2023; revised 10 July 2023 and 20 September 2023; accepted 17 October 2023. Date of publication 30 October 2023; date of current version 6 December 2023. This work was supported in part by the National Natural Science Foundation of China under Grants 52105079 and 62103455, and in part by the Research Fund of Guangdong-Hong Kong-Macao Joint Laboratory for Intelligent Micro-Nano Optoelectronic Technology under Grant 2020B1212030010. Recommended for publication by Associate Editor N. R. N. Idris. *(Corresponding author: Guodong Feng.)*

Kaide Huang is with the School of Mathematics and Big Data, Foshan University, Foshan 528000, China (e-mail: kaidehuang@fosu.edu.cn).

Beichen Ding is with the School of Advanced Manufacturing, Sun Yat-sen University, Shenzhen 518107, China (e-mail: dingbch@mail.sysu.edu.cn).

Chunyan Lai is with the Department of Electrical and Computer Engineering, Concordia University, Montreal, QC H3G 1M8, Canada (e-mail: chunyan.lai@concordia.ca).

Guodong Feng is with the School of Intelligent Systems Engineering, Sun Yat-sen University, Shenzhen 518107, China (e-mail: qqfengguodong@gmail.com).

Color versions of one or more figures in this article are available at https://doi.org/10.1109/TPEL.2023.3327956.

Digital Object Identifier 10.1109/TPEL.2023.3327956

I. Introduction

IN PERMANENT magnet synchronous machine (PMSM) drives, the temperature of magnet is a crucial parameter for high-performance control and condition monitoring [1], [2], [3], [4], [5]. The magnet flux linkage decreases as the temperature of magnet increases. Therefore, accurate magnet temperature can be used to compensate the flux linkage reduction due to temperature rise for high precision torque control. The magnet temperature can also be utilized to monitor the health status of permanent magnet in the rotor, preventing excessive overheating and avoiding damage to the magnet and machine. Hence, this article investigates accurate modeling and estimation of magnet temperature for high performance control of PMSMs.

Magnet temperature estimation has been widely studied in the literature. Generally, there are mainly two approaches to estimate magnet temperature. One is based on the thermal network analysis and the other is based on tracking the temperature-dependent parameter variation, such as the magnet flux linkage. The thermal network-based approach models the heat flow in the machine, enabling the calculation of the temperature for any part of the machine. For instance, in [6], [7], [8], [9], and [10], the lumped parameter thermal network (LPTN) is proposed for the PMSM to estimate the magnet temperature. This approach either requires geometric information or accurate loss data in order to train the network and calculate the temperature of the motor parts, which inevitably limits its applicability in certain practical applications.

The parameter variation-based approach belongs to the machine model-based approaches, which rely on the machine model to build an estimation model for tracking the variation of parameters and estimating magnet temperature. Both high-frequency (HF) and fundamental models are explored for this purpose. In the HF model-based approach, an HF signal is injected into the machine to induce an HF response, from which temperature-dependent parameters can be extracted. For instance, HF currents are injected in [11], [12], and [13], and HF voltages are injected in [14], [15], and [16] to extract the HF resistance for magnet temperature estimation. In [17] and [18], the HF inductance is explored for magnet temperature estimation, and speed harmonics are also extracted to track the

variation of the magnet flux linkage for temperature estimation purpose [19]. The HF model-based approaches can effectively reduce the influence from the fundamental components and thus achieve improved performance under low speed conditions. However, injecting an HF signal consumes inverter voltage, thereby affecting the maximum achievable speed. In addition, it introduces HF noise and extra losses that are unsuitable for certain applications. In fundamental model-based approach, the flux linkage tracking model is derived from the machine model to estimate magnet temperature. For instance, the magnet temperature is estimated from the PWM measurements using the fundamental model in [20] and [21]. The variation of rotor flux linkage with respect to the injected position offset is presented in [22]. Moreover, the variation of inductance is considered in the fundamental model for magnet temperature estimation [23]. To improve the estimation performance, various strategies are proposed to deal with the magnetic saturation and inverter distortion. For instance, the position offset is added in [24] to compensate the inverter distortion and nonlinear saturation model is employed in [25], [26], and [27] to compensate the magnetic saturation. The fundamental model-based approach is noninvasive and can estimate the temperature using available measurements, making it applicable in most scenarios.

The accuracy of the machine model deteriorates under high-speed conditions due to the core loss effect, which is because the core loss becomes comparable in magnitude to the copper loss and cannot be neglected [28], [29], [30], [31], [32]. However, existing approaches have not considered the core loss effect, and thus their performance will deteriorate under high-speed conditions. Therefore, it is critical to consider the core loss effect to improve estimation accuracy under high-speed conditions. The core loss effect is highly nonlinear and dependent on both load conditions and motor speeds. The widely used core loss model introduces the core loss resistance into the machine model, which has been employed for high performance control including maximum efficiency control in [33]. However, it is challenging to obtain accurate core loss resistance due to the highly nonlinear behavior. Hence, directly extending the existing core loss model to temperature estimation will complicate the model and implementation. On the other hand, the data-driven approach brings the machine learning techniques into temperature estimation, which can eliminate the need of precise machine models [34]. This inspires us to develop the data-driven model to compensate the core loss effect for estimation performance improvement.

This article proposes a novel hybrid approach combining both the fundamental model and the data-driven based model for accurate magnet temperature estimation. To cancel the inverter distortion effect, the flux linkages in the fundamental model are projected into a new frame to establish the relationship between the flux linkages and magnet temperature. Considering the effect of core loss introduces nonlinear distortions to the original fundamental model, and compensating for the model offsets due to core loss is necessary. To achieve this, a radial basis function (RBF)-based network is employed. As the core loss induced offsets are complex and nonlinear, their models are derived from the proposed estimation model to obtain the required data for training the network. The major contributions include deriving an estimation model that takes into account core loss and eliminates the effects of winding resistance variation and inverter distortion for temperature estimation; developing a data-driven model based on RBF network to compensate the core loss effect. With core loss compensation, the proposed approach can effectively improve estimation performance especially under the high-speed conditions, which are validated with extensive experiments and comparisons on a laboratory interior PMSM drive.

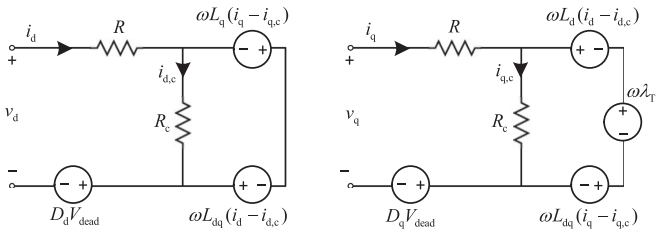

Fig. 1. PMSM equivalent circuit model considering the core loss and inverter nonlinearity.

II. PM Temperature Estimation Model Using Virtual Flux With Core Loss Awareness

This section first presents permanent magnet temperature hybrid modeling and estimation based on virtual flux linkage tracking and core loss compensation, then discusses the effect of inductance variation and time delay on the temperature estimation.

A. Hybrid Modeling and Estimation

For PMSM, the equivalent circuit model considering the core loss and voltage source inverter (VSI) nonlinearity is presented in Fig. 1. The equivalent core loss resistance R_c depends on the speed and *dq*-axis currents. The core loss is significant when the rotor speed is close to or higher than the rated speed. Based on the circuit model, the fundamental steady-state machine equations can be expressed as

$$\begin{cases} v_d = Ri_d - \omega F_q + D_d V_{dead} \\ v_q = Ri_q + \omega F_d + D_q V_{dead} \end{cases} \tag{1}$$

with

$$\begin{cases} F_d = L_d(i_d - i_{d,c}) + L_{dq}(i_q - i_{q,c}) + \lambda_T \\ F_q = L_q(i_q - i_{q,c}) + L_{dq}(i_d - i_{d,c}) \end{cases} \tag{2}$$

where $i_{d/q}$, $v_{d/q}$, and $F_{d/q}$ are the *d*/*q*-axis current, voltage, flux linkage; R is the stator winding resistance; ω is the rotor speed; $L_{d/q}$ is the *d*/*q*-axis self-saturation inductance, L_{dq} is the *dq*-axis cross-saturation inductance; $i_{d/q,c}$ is the core loss current; λ_T is the PM flux linkage that is a function of the PM temperature; V_{dead} is the inverter distortion voltage caused by the dead-time effect, $D_{d/q}$ is the nonlinear distorted coefficient depending on the current angle γ and rotor position θ

$$\begin{cases} D_d = 2\sin(\theta - \text{int}\{3(\theta + \gamma + \pi/6)/\pi\} \times \pi/3) \\ D_q = 2\cos(\theta - \text{int}\{3(\theta + \gamma + \pi/6)/\pi\} \times \pi/3) \end{cases} \tag{3}$$

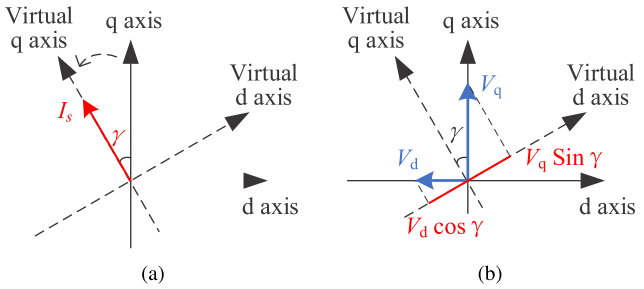

Fig. 2. Diagram of reference frame transformation. (a) Virtual *dq*-axis. (b) Projected voltage on the virtual *d*-axis.

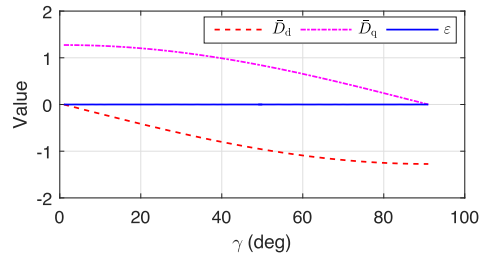

Fig. 3. Values of $\bar{D}_\mathrm{d}$, $\bar{D}_\mathrm{q}$, and $\varepsilon = (\bar{D}_\mathrm{q}\sin\gamma + \bar{D}_\mathrm{d}\cos\gamma)$.

where $\mathrm{int}\{x\}$ is a function of taking the nearest integer of x.

Since $D_{\mathrm{d/q}}$ changes periodically with respect to the rotor position, which is generally unavailable, the short-term average value of $D_{\mathrm{d/q}}$ is utilized to eliminate the effect of the rotor position. Consequently, (1) and (2) can be rewritten as

$$\begin{cases} V_\mathrm{d} = RI_\mathrm{d} - \omega F_\mathrm{q} + \bar{D}_\mathrm{d} V_\mathrm{dead} \\ V_\mathrm{q} = RI_\mathrm{q} + \omega F_\mathrm{d} + \bar{D}_\mathrm{q} V_\mathrm{dead} \end{cases} \tag{4}$$

with

$$\begin{cases} F_\mathrm{d} = L_\mathrm{d}(I_\mathrm{d} - I_\mathrm{d,c}) + L_\mathrm{dq}(I_\mathrm{q} - I_\mathrm{q,c}) + \lambda_\mathrm{T} \\ F_\mathrm{q} = L_\mathrm{q}(I_\mathrm{q} - I_\mathrm{q,c}) + L_\mathrm{dq}(I_\mathrm{d} - I_\mathrm{d,c}) \end{cases} \tag{5}$$

where $V_{\mathrm{d/q}}$, $I_{\mathrm{d/q}}$, $I_{\mathrm{d/q,c}}$, and $\bar{D}_{\mathrm{d/q}}$ are the average values of $v_{\mathrm{d/q}}$, $i_{\mathrm{d/q}}$, $i_{\mathrm{d/q,c}}$, and $D_{\mathrm{d/q}}$ over multiple electrical cycles, respectively. By calculating the definite integral of (3) with respect to θ in an electrical cycle, it can be derived that

$$\begin{cases} \bar{D}_d = -6\left[\cos(\pi/6-\gamma) - \cos(\pi/6+\gamma)\right]/\pi \\ \bar{D}_q = 6\left[\sin(\pi/6-\gamma) + \sin(\pi/6+\gamma)\right]/\pi. \end{cases} \tag{6}$$

The values of $\bar{D}_d$ and $\bar{D}_q$ vary with the current angle γ, but are independent of the rotor position θ. In addition, the *dq*-axis currents and core loss currents can be expressed in the form of amplitude and phase angle

$$\begin{aligned} I_\mathrm{d} &= -I_\mathrm{s}\sin\gamma, I_\mathrm{q} = I_\mathrm{s}\cos\gamma \\ I_\mathrm{d,c} &= -I_\mathrm{s,c}\sin\alpha, I_\mathrm{q,c} = I_\mathrm{s,c}\cos\alpha \end{aligned} \tag{7}$$

where I_s and $I_\mathrm{s,c}$ are the amplitudes of stator current and core loss current, respectively, α is the core loss angle. From Fig. 1, we have $I_\mathrm{d,c}/I_\mathrm{q,c} = -F_\mathrm{q}/F_\mathrm{d}$. Therefore, α is determined by $\arctan(F_\mathrm{q}/F_\mathrm{d})$, which depends on the *dq*-axis flux linkages.

Consider the virtual *dq*-axis, which is obtained by rotating the actual *dq*-axis counterclockwise by the angle γ, as shown in Fig. 2(a). The virtual *d*-axis is at 90° from the stator current vector. It can be observed from Fig. 2(b) that the projected voltage on the virtual *d*-axis is $V_\mathrm{q}\sin\gamma + V_\mathrm{d}\cos\gamma$. Multiplying the two equations in (4) by $\cos\gamma$ and $\sin\gamma$, respectively, leads to

$$\begin{cases} V_\mathrm{d}\cos\gamma = RI_\mathrm{d}\cos\gamma - \omega F_\mathrm{q}\cos\gamma + \bar{D}_\mathrm{d}\cos\gamma V_\mathrm{dead} \\ V_\mathrm{q}\sin\gamma = RI_\mathrm{q}\sin\gamma + \omega F_\mathrm{d}\sin\gamma + \bar{D}_\mathrm{q}\sin\gamma V_\mathrm{dead}. \end{cases} \tag{8}$$

Since the stator current vector is perpendicular to the virtual *d*-axis, we can derive the virtual voltage based on (7) and (8)

$$\begin{aligned} V_\mathrm{q}\sin\gamma + V_\mathrm{d}\cos\gamma &= R(-I_\mathrm{s}\sin\gamma\cos\gamma + I_\mathrm{s}\cos\gamma\sin\gamma) \\ &\quad + \omega(F_\mathrm{d}\sin\gamma - F_\mathrm{q}\cos\gamma) + \varepsilon V_\mathrm{dead} \\ &= \omega(F_\mathrm{d}\sin\gamma - F_\mathrm{q}\cos\gamma) + \varepsilon V_\mathrm{dead} \end{aligned} \tag{9}$$

where

$$\varepsilon = \bar{D}_\mathrm{q}\sin\gamma + \bar{D}_\mathrm{d}\cos\gamma. \tag{10}$$

From (9), the effect of the stator resistance on the virtual *d*-axis is eliminated. Moreover, substituting (6) into (10), we have

$$\begin{aligned} \varepsilon &= 6/\pi\left[\sin(\pi/6-\gamma)\sin\gamma + \sin(\pi/6+\gamma)\sin\gamma\right] + \\ &\quad - 6/\pi\left[\cos(\pi/6-\gamma)\cos\gamma - \cos(\pi/6+\gamma)\cos\gamma\right] \\ &= 0. \end{aligned} \tag{11}$$

It can be seen that by combining nonlinear coefficients $\bar{D}_\mathrm{d}$ and $\bar{D}_\mathrm{q}$, the constant term $\varepsilon = 0$ can be obtained. Fig. 3 shows the numerical results of $\bar{D}_\mathrm{d}$, $\bar{D}_\mathrm{q}$, and ε, which further demonstrates the advantage of the virtual *d*-axis in eliminating nonlinear effects of the inverter. Then, (9) can be simplified as

$$V_\mathrm{q}\sin\gamma + V_\mathrm{d}\cos\gamma = \omega F_\mathrm{v} \tag{12}$$

where $F_\mathrm{v} = F_\mathrm{d}\sin\gamma - F_\mathrm{q}\cos\gamma$, which is the virtual flux linkage after projection.

Remark 1: The benefits of constructing virtual axis are twofold. On the one hand, the virtual *d*-axis voltage is independent of the winding resistance R, and the effect of resistance variation induced by the winding temperature can be eliminated. On the other hand, the terms $\bar{D}_\mathrm{d}$, $\bar{D}_\mathrm{q}$, and V_dead associated with the inverter distortion effect can be eliminated to improve the accuracy and computational efficiency of PM temperature estimation. Indeed, both of the effects of stator resistance and inverter distortion are in phase with the stator current, and perpendicular to the virtual *d*-axis, thus they are independent of projection components on the virtual *d*-axis.

Based on (5) and (7), the virtual flux linkage F_v can be expressed as

$$\begin{aligned} F_\mathrm{v} &= F_\mathrm{d}\sin\gamma - F_\mathrm{q}\cos\gamma \\ &= \lambda_\mathrm{T}\sin\gamma - I_\mathrm{s}\left(L_\mathrm{d}\sin^2\gamma + L_\mathrm{q}\cos^2\gamma - L_\mathrm{dq}\sin 2\gamma\right) \\ &\quad + I_\mathrm{s,c}(L_\mathrm{d}\sin\alpha\sin\gamma + L_\mathrm{q}\cos\alpha\cos\gamma - L_\mathrm{dq}\sin(\alpha+\gamma)) \end{aligned} \tag{13}$$

where the first term is associated with the PM flux linkage, which varies with the PM temperature; the second is the inductance-dependent term that is affected by magnetic saturation and cross coupling; the third term depends on complex core loss effect.

As mentioned previously, the equivalent core loss resistance R_c varies with both the speed and the stator current, especially under high-speed operating conditions. From Fig. 1, it is observed that the voltage on R_c depends on the speed, the currents and the inductances, in which all the inductances including L_d, L_q, and L_{dq} can be modeled by the stator current. Thus, the core loss current can be represented as unknown functions of the speed and current, that is, $I_{s,c} = g_I(\omega, I_s, \gamma)$, $\alpha = g_\alpha(\omega, I_s, \gamma)$.

Consider the virtual flux linkage at the following two PM temperatures.

1) At time t, the PM temperature is T_t, the PM flux linkage is λ_T^t, the motor speed is ω_t, the current magnitude and angle are $I_{s,t}$ and γ_t, respectively, the virtual flux linkage is denoted as F_v^t and given by

$$\begin{aligned} F_v^t =& \lambda_T^t \sin\gamma_t - I_{s,t}\left(L_d \sin^2\gamma_t + L_q \cos^2\gamma_t - L_{dq}\sin 2\gamma_t\right) \\ &+ I_{s,c}^t(L_d \sin\alpha_t \sin\gamma_t + L_q \cos\alpha_t \cos\gamma_t - L_{dq}\sin(\alpha_t+\gamma_t)) \end{aligned} \tag{14}$$

where $I_{s,c}^t = g_I(\omega_t, I_{s,t}, \gamma_t)$, $\alpha_t = g_\alpha(\omega_t, I_{s,t}, \gamma_t)$.

2) At initial time t_0, the PM temperature is T_0, the PM flux linkage is λ_T^0, the motor speed is ω_0, the virtual flux linkage under the current condition $\{I_{s,t}, \gamma_t\}$ is denoted as $F_v^0(I_{s,t}, \gamma_t)$ and given by

$$\begin{aligned} &F_v^0(I_{s,t}, \gamma_t) \\ &= \lambda_T^0 \sin\gamma_t - I_{s,t}\left(L_d \sin^2\gamma_t + L_q \cos^2\gamma_t - L_{dq}\sin 2\gamma_t\right) \\ &+ I_{s,c}^0(L_d \sin\alpha_0 \sin\gamma_t + L_q \cos\alpha_0 \cos\gamma_t - L_{dq}\sin(\alpha_0+\gamma_t)) \end{aligned} \tag{15}$$

where $I_{s,c}^0 = g_I(\omega_0, I_{s,t}, \gamma_t)$, $\alpha_0 = g_\alpha(\omega_0, I_{s,t}, \gamma_t)$.

The difference between F_v^t and $F_v^0(I_{s,t}, \gamma_t)$ is

$$F_v^t - F_v^0(I_{s,t}, \gamma_t) = \Delta\lambda_T^t \sin\gamma_t + \Delta F_{v,c}^t \tag{16}$$

where $\Delta\lambda_T^t$ is the flux variation induced by PM temperature

$$\Delta\lambda_T^t = \lambda_T^t - \lambda_T^0 \tag{17}$$

and $\Delta F_{v,c}^t$ is the flux variation induced by core loss

$$\begin{aligned} \Delta F_{v,c}^t =& I_{s,c}^t(L_d \sin\alpha_t \sin\gamma_t + L_q \cos\alpha_t \cos\gamma_t - L_{dq}\sin(\alpha_t+\gamma_t)) \\ &- I_{s,c}^0(L_d \sin\alpha_0 \sin\gamma_t + L_q \cos\alpha_0 \cos\gamma_t - L_{dq}\sin(\alpha_0+\gamma_t)). \end{aligned} \tag{18}$$

Using (16), we have

$$\Delta\lambda_T^t = \left(F_v^t - F_v^0(I_{s,t}, \gamma_t) - \Delta F_{v,c}^t\right) / \sin\gamma_t. \tag{19}$$

Following the studies in [25], [35], the linear thermal model of the PM flux linkage can be expressed as

$$\lambda_T^t = \lambda_T^0(1 + \beta(T_t - T_0)) \tag{20}$$

where β is the thermal coefficient, and its value is about $-0.12\%/\,^\circ$C for the magnet made of the NdFeB material. From (17), (19), and (20), the hybrid PM temperature estimation model is given by

$$\begin{aligned} T_t &= T_0 + \Delta\lambda_T^t / \left(\beta\lambda_T^0\right) \\ &= T_0 + \left(F_v^t - F_v^0(I_{s,t}, \gamma_t) - \Delta F_{v,c}^t\right) / \left(\beta\lambda_T^0 \sin\gamma_t\right). \end{aligned} \tag{21}$$

In (21), F_v^t can be online calculated from the collected $V_{d,t}$, $V_{q,t}$, ω_t, $I_{s,t}$, and γ_t at time t by using (12)

$$F_v^t = (V_{q,t} \sin\gamma_t + V_{d,t} \cos\gamma_t)/\omega_t. \tag{22}$$

$F_v^0(I_{s,t}, \gamma_t)$ is the reference flux at the given current $\{I_{s,t}, \gamma_t\}$ under the condition of initial ω_0 and T_0. In order to obtain the value of $F_v^0(I_{s,t}, \gamma_t)$, the F_v^0 map with respect to arbitrary I_s and γ needs to be built in advance. This can be achieved by a data-driven method using the offline experimental data at the speed of ω_0 and the PM temperature of T_0, such as at the room temperature. The details are presented in the next section. In addition, $\Delta F_{v,c}^t$ is the term of core loss compensation presented in (18). As can be seen that $\Delta F_{v,c}^t$ depends on $I_{s,c}^t$, $I_{s,c}^0$, α_t, α_0, L_d, L_q, and L_{dq}, which are functions of ω_t, ω_0, $I_{s,t}$, and γ_t. Thus, $\Delta F_{v,c}^t$ can be denoted as

$$\Delta F_{v,c}^t = G(I_{s,t}, \gamma_t, \Delta\omega_t) \tag{23}$$

where $G(\cdot)$ represents a function, $\Delta\omega_t = \omega_t - \omega_0$, ω_0 can be regarded as the reference speed. To obtain the value of $\Delta F_{v,c}^t$, the core loss compensation model $\Delta F_{v,c} = G(I_s, \gamma, \Delta\omega)$ should be built, which is also achieved by a data-driven method and presented in the next section. In summary, by tracking the variation of virtual flux linkage at $\{I_{s,t}, \gamma_t\}$ and compensating the core loss term induced by motor speed, the PM temperature T_t can be estimated using (21).

Remark 2: The hybrid estimation model (21) consists of the flux linkage variation-dependent term and the data-driven core loss compensation term. The former is obtained by tracking the change of voltage measurements without estimating machine parameters, which is computationally efficient and practical. The latter can deal with the model offset caused by core loss effect, thus improving temperature estimation accuracy.

B. Discussions

1) Effect of Inductance Variation: Based on (14) and (15), the difference of F_v^t and $F_v^0(I_{s,t}, \gamma_t)$ considering the inductance variation caused by the magnet temperature can be derived as

$$\begin{aligned} &F_v^t - F_v^0(I_{s,t}, \gamma_t) = \Delta\lambda_T^t \sin\gamma_t + \Delta F_{v,c}^t \\ &+ I_{s,t}\left(\Delta L_d \sin^2\gamma_t + \Delta L_q \cos^2\gamma_t - \Delta L_{dq}\sin 2\gamma_t\right) \\ &+ I_{s,c}^t(\Delta L_d \sin\alpha_t \sin\gamma_t + \Delta L_q \cos\alpha_t \cos\gamma_t - \Delta L_{dq}\sin(\alpha_t+\gamma_t)) \end{aligned} \tag{24}$$

where ΔL_d, ΔL_q, and ΔL_{dq} are the inductance variations when the PM temperature varies from T_0 to T_t. Since the core loss current is a small component of the stator current (i.e., $I_{s,c}^t \ll I_{s,t}$), the last term in (24) is negligible compared to the third term. Thus, (24) can be simplified as

$$\begin{aligned} &F_v^t - F_v^0(I_{s,t}, \gamma_t) = \Delta\lambda_T^t \sin\gamma_t + \Delta F_{v,c}^t \\ &+ I_{s,t}\left(\Delta L_d \sin^2\gamma_t + \Delta L_q \cos^2\gamma_t - \Delta L_{dq}\sin 2\gamma_t\right). \end{aligned} \tag{25}$$

It can be observed from (16) and (25) that the difference is adding the inductance variation term induced by the magnet temperature.

To analyze the effect of inductance variation, an experimental observation is conducted in Test 4, in which the speed and the

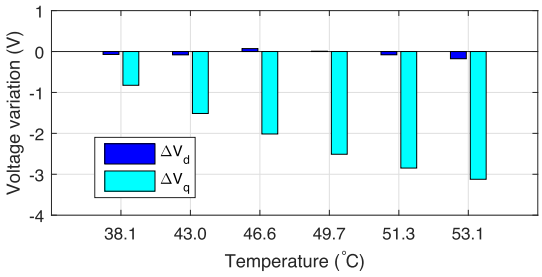

Fig. 4. Voltage variation with respect to the PM temperature.

stator current are fixed, and the *dq*-axis voltages are collected at different PM temperatures. The experimental setup is detailed in Section IV-B. The initial reference voltages are obtained at the PM temperature of 30.7 °C. Fig. 4 shows the variations of *dq*-axis voltages (ΔV_d and ΔV_q) with respect to the PM temperature. From (4), it can be observed that in addition to the change of winding resistance, ΔV_d is mainly affected by $\Delta L_{\rm q}$, while ΔV_q is determined by $\Delta\lambda_{\rm T}$ and $\Delta L_{\rm d}$. As can be seen in Fig. 4, the amplitudes of ΔV_d are small, indicating that the change of $L_{\rm q}$ is relatively small, and its effect on ΔV_d may be partially offset by the variation of winding resistance. Moreover, ΔV_q varies significantly with the PM temperature, in which $\Delta\lambda_{\rm T}$ caused by the PM temperature can be regarded as the dominant factor. The temperature induced inductance variation is ignored in this work. Indeed, if the relationship between inductance and temperature is accurately modeled, the more accurate temperature estimation model can be achieved from (25). The linear inductance variation model has been explored in the literature [23], but more efforts are required to improve model accuracy and usability when the cross coupling and core loss are considered, which will be explored in the further work.

2) Effect of Unit Sample Time Delay: For current controller-based drive system, the execution of control algorithm and the modulation of PWM induce a time delay of one and a half sampling periods in the PWM output [36], [37], which leads to the phase shift $e^{-j(1.5T_s\omega)}$ in the voltage vector, where T_s is the sampling period. Thus, (4) can be expressed as

$$\begin{cases} V_{\rm d}^{\rm s} = RI_{\rm d} - \omega F_{\rm q} + \bar{D}_{\rm d}^{\rm s} V_{\rm dead} \\ V_{\rm q}^{\rm s} = RI_{\rm q} + \omega F_{\rm d} + \bar{D}_{\rm q}^{\rm s} V_{\rm dead} \end{cases} \tag{26}$$

where $V_{\rm dq}^{\rm s} = V_{\rm d}^{\rm s} + jV_{\rm q}^{\rm s}$ and $\bar{D}_{\rm dq}^{\rm s} = \bar{D}_{\rm d}^{\rm s} + j\bar{D}_{\rm q}^{\rm s}$ are the voltage and VSI distortion vectors after phase shift in the static reference frame, respectively

$$V_{\rm dq}^{\rm s} = V_{\rm dq} e^{-j(1.5T_s\omega)},\ \bar{D}_{\rm dq}^{\rm s} = \bar{D}_{\rm dq} e^{-j(1.5T_s\omega)} \tag{27}$$

where $V_{\rm dq} = V_{\rm d} + jV_{\rm q}$, $\bar{D}_{\rm dq} = \bar{D}_{\rm d} + j\bar{D}_{\rm q}$. Based on (26), we can rewrite (9) as

$$\begin{aligned} V_{\rm q}^{\rm s}\sin\gamma + V_{\rm d}^{\rm s}\cos\gamma &= R(-I_{\rm s}\sin\gamma\cos\gamma + I_{\rm s}\cos\gamma\sin\gamma) \\ &\quad + \omega(F_{\rm d}\sin\gamma - F_{\rm q}\cos\gamma) + \varepsilon^{\rm s} V_{\rm dead} \\ &= \omega(F_{\rm d}\sin\gamma - F_{\rm q}\cos\gamma) + \varepsilon^{\rm s} V_{\rm dead} \end{aligned} \tag{28}$$

where

$$\varepsilon^{\rm s} = \bar{D}_{\rm q}^{\rm s}\sin\gamma + \bar{D}_{\rm d}^{\rm s}\cos\gamma. \tag{29}$$

It can be seen from (28) that the stator resistance R can be eliminated, similar to the case without considering time delay in (9). Further, based on (27), we have

$$\begin{aligned} \bar{D}_{\rm dq}^{\rm s} &= \left(\bar{D}_{\rm d} + j\bar{D}_{\rm q}\right) e^{-j(1.5T_s\omega)} \\ &= \underbrace{\left(\bar{D}_{\rm d}\cos(1.5T_s\omega) + \bar{D}_{\rm q}\sin(1.5T_s\omega)\right)}_{\bar{D}_{\rm d}^{\rm s}} \\ &\quad + j\underbrace{\left(\bar{D}_{\rm q}\cos(1.5T_s\omega) - \bar{D}_{\rm d}\sin(1.5T_s\omega)\right)}_{\bar{D}_{\rm q}^{\rm s}}. \end{aligned} \tag{30}$$

Substituting $\bar{D}_{\rm d}^{\rm s}$ and $\bar{D}_{\rm q}^{\rm s}$ into (29), and then incorporating (6) into it yields

$$\begin{aligned} \varepsilon^{\rm s} &= \bar{D}_{\rm q}\sin(\gamma + 1.5T_s\omega) + \bar{D}_{\rm d}\cos(\gamma + 1.5T_s\omega) \\ &= \frac{\pi}{6}\sin(1.5T_s\omega). \end{aligned} \tag{31}$$

Substituting (31) into (28), we have

$$V_{\rm q}^{\rm s}\sin\gamma + V_{\rm d}^{\rm s}\cos\gamma = \omega F_{\rm v} + \frac{\pi}{6}\sin(1.5T_s\omega)V_{\rm dead}. \tag{32}$$

From (27), $V_{\rm dq}^{\rm s}$ can be expressed as

$$\begin{aligned} V_{\rm dq}^{\rm s} &= (V_{\rm d} + jV_{\rm q})e^{-j(1.5T_s\omega)} \\ &= \underbrace{\left(V_{\rm d}\cos(1.5T_s\omega) + V_{\rm q}\sin(1.5T_s\omega)\right)}_{V_{\rm d}^{\rm s}} \\ &\quad + j\underbrace{\left(V_{\rm q}\cos(1.5T_s\omega) - V_{\rm d}\sin(1.5T_s\omega)\right)}_{V_{\rm q}^{\rm s}}. \end{aligned} \tag{33}$$

Substituting (33) into (32) yields

$$\begin{aligned} &V_{\rm q}\sin(\gamma + 1.5T_s\omega) + V_{\rm d}\cos(\gamma + 1.5T_s\omega) \\ &= \omega F_{\rm v} + \frac{\pi}{6}\sin(1.5T_s\omega)V_{\rm dead}. \end{aligned} \tag{34}$$

Comparing (34) with (12), it can be observed that the phase shift angle $1.5T_s\omega$ and the inverter distortion term are introduced in the case of considering time delay.

Based on (19), (23), and (34), the temperature-induced flux variation considering time delay effect can be represented as

$$\Delta\lambda_{\rm T}^{t,{\rm s}} = (F_{\rm v}^{t,{\rm s}} - F_{\rm v}^{0,{\rm s}}(I_{{\rm s},t},\gamma_t) - G(I_{{\rm s},t},\gamma_t^{\rm s},\Delta\omega_t) + e)/\sin\gamma_t \tag{35}$$

where

$$\begin{aligned} F_{\rm v}^{t,{\rm s}} &= (V_{{\rm q},t}\sin(\gamma_t + 1.5T_s\omega_t) + V_{{\rm d},t}\cos(\gamma_t + 1.5T_s\omega_t))/\omega_t \\ F_{\rm v}^{0,{\rm s}}(I_{{\rm s},t},\gamma_t) &= (V_{{\rm q},0}\sin(\gamma_t + 1.5T_s\omega_0) \\ &\quad + V_{{\rm d},0}\cos(\gamma_t + 1.5T_s\omega_0))/\omega_0 \\ \gamma_t^{\rm s} &= \gamma_t + 1.5T_s\omega \\ e &= \frac{\pi}{6}V_{\rm dead}\left(\sin(1.5T_s\omega_0)/\omega_0 - \sin(1.5T_s\omega_t)/\omega_t\right). \end{aligned} \tag{36}$$

In practice, the phase shift angle $1.5T_s\omega$ is small. For example, $T_s = 0.5\times10^{-4}$ s in our experimental drive system, and $1.5T_s\omega = 0.0188$ rad at the speed of 600 rpm. Thus, $\sin(1.5T_s\omega) \approx 1.5T_s\omega$ using Taylor expansion. The term e

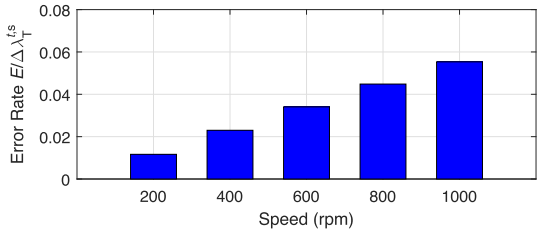

Fig. 5. Error rate caused by time delay effect in the experimental platform.

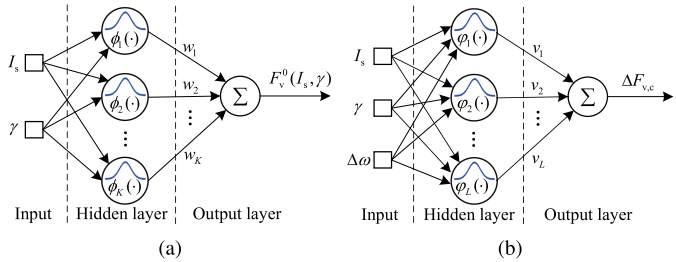

Fig. 6. Graphical models of $F_{\rm v}^0$ and $\Delta F_{\rm v,c}$ based on RBF networks. (a) $F_{\rm v}^0$. (b) $\Delta F_{\rm v,c}$.

associated with inverter distortion can be expressed as $e \approx \pi/6 V_{\rm dead}(1.5T_s\omega_0/\omega_0 - 1.5T_s\omega_t/\omega_t) = 0$. It implies that the effect of nonlinear inverter distortion can still be basically eliminated even considering unit sample time delay.

It can be observed from (19) and (35) that the dominant error of flux variation on establishing temperature estimation models with and without considering time delay is

$$E = \Delta\lambda_{\rm T}^{t,{\rm s}} - \Delta\lambda_{\rm T}^{t} = \left[\left(F_{\rm v}^{t,{\rm s}} - F_{\rm v}^{0,{\rm s}}(I_{{\rm s},t},\gamma_t)\right) - \left(F_{\rm v}^{t} - F_{\rm v}^{0}(I_{{\rm s},t},\gamma_t)\right)\right] / \sin\gamma_t. \quad (37)$$

Without loss of generality, the reference speed ω_0 is assumed to be the same as the current speed ω_t, and then E can be simplified by substituting (22) and (36) into (37) as follows:

$$E = (V_{{\rm q},t} - V_{{\rm q},0})\left(\sin(\gamma_t + 1.5T_e\omega_t) - \sin\gamma_t\right)/(\omega_t \sin\gamma_t) \quad (38)$$

in which $V_{{\rm d},t}$ is independent of temperature change, and the terms depending on $(V_{{\rm d},t} - V_{{\rm d},0})$ can be eliminated. As discussed previously, $1.5T_s\omega_t$ is small, and thus the error E is also small. Fig. 5 shows the error rate $E/\Delta\lambda_{\rm T}^{t,{\rm s}}$ with the machine parameters of our experimental platform, in which γ_t is fixed to 28°. As can be seen, the error rate increases with the increase of motor speed, but their values remain small at different speeds, being less than 5.54%. Ignoring the time delay effect may introduce a relatively small error in temperature estimation. To eliminate the influence of time delay and improve the accuracy of temperature estimation, one should compensate the voltage output for the PMSM with $e^{1.5T_e\omega}$ in the drive system. By doing so, the effect of both winding resistance and VSI nonlinearity can be eliminated completely.

III. Data-Driven-Based Virtual Flux and Core Loss Compensation Modeling

This section presents the modeling of the reference virtual flux $F_{\rm v}^0$ and the core loss induced flux compensation $\Delta F_{\rm v,c}$. Due to the high nonlinearity and complexity of motor system caused by magnetic saturation, core loss, etc., it is limited to describe $F_{\rm v}^0$ and $\Delta F_{\rm v,c}$ with mechanism models. In this work, a data-driven method based on RBF neural network is explored to model them.

A. Virtual Flux F_v^0 Modeling

At PM temperature T_0, $\lambda_{\rm T}^0$ is a constant. For a fixed $\lambda_{\rm T}^0$ and ω_0, $F_{\rm v}^0$ varies with the current $\{I_{\rm s}, \gamma\}$ due to magnetic saturation. The graphical representation of $F_{\rm v}^0(I_{\rm s},\gamma)$ based on an RBF network is presented in Fig. 6(a). In the hidden layer, K Gaussian functions with different centers are adopted to measure the approximation between the input and each center. These approximate measures are then weighted and summed to output $F_{\rm v}^0$, that is

$$F_{\rm v}^0(I_{\rm s},\gamma) = \sum_{j=1}^{K} w_j \phi_j\left([I_{\rm s},\gamma]^{\rm T}\right) \quad (39)$$

with

$$\phi_j\left([I_{\rm s},\gamma]^{\rm T}\right) = \exp\left(-\frac{(I_{\rm s}-I_{{\rm s},j})^2 + (\gamma-\gamma_j)^2}{2\sigma_j^2}\right) \quad (40)$$

where w_j is the jth weight coefficient, $(I_{{\rm s},j},\gamma_j)$ is the center of $\phi_j(\cdot)$, σ_j is the scale parameter, and in general, $\sigma_j = \sigma$ for $j = 1, 2\cdots, K$. In other words, all Gaussian functions have the same scale parameter σ, which can be regarded as a tuning parameter in the algorithm. It should be noted that the model (39) can provide strong self-learning ability for nonlinear approximation, which is able to describe the nonlinear variation caused by magnetic saturation.

The key of modeling $F_{\rm v}^0$ is to estimate the RBF centers $\{I_{{\rm s},j},\gamma_j\}_{j=1}^K$ and the weight coefficients $\{w_j\}_{j=1}^K$. For this purpose, an offline experimental test can be conducted. The motor speed is fixed to ω_0, and the PM temperature is at room temperature T_0. The dq-axis voltages $\{V_{{\rm d},i}^0\}_{i=1}^N$ and $\{V_{{\rm q},i}^0\}_{i=1}^N$ are collected under N different current conditions $\{I_{{\rm s},i},\gamma_i\}_{i=1}^N$. Since the PM temperature varies slowly with time and the data collection is completed in a short period of time, the PM temperature is considered to remain unchanged at T_0 in the test. Based on (12), we have

$$F_{\rm v}^0(I_{{\rm s},i},\gamma_i) = \left(V_{{\rm q},i}^0 \sin\gamma_i + V_{{\rm d},i}^0 \cos\gamma_i\right)/\omega_0. \quad (41)$$

Then, the training data including the inputs $\{I_{{\rm s},i},\gamma_i\}_{i=1}^N$ and the outputs $\{F_{\rm v}^0(I_{{\rm s},i},\gamma_i)\}_{i=1}^N$ can be constructed for parameter estimation of the RBF network. In this work, K-means and recursive least squares algorithms are adopted for RBF center and weight coefficient estimation, respectively, which can be implemented using MATLAB neural network toolbox. During the training process, the size of the hidden layer (K) is increased until the network expectation error is satisfied. For the experimental studies presented in Section IV, K is about 20 with given the expected error of 10^{-6}. In fact, the estimated results are less

sensitive to K, and a reasonable value of K can be specified if the training is implemented in an industrial controller.

B. Core Loss Compensation $\Delta F_{v,c}$ Modeling

As discussed in (23), the core loss induced compensation term $\Delta F_{\mathrm{v,c}}$ is a function of I_{s}, γ and $\Delta\omega$. Such a function is unknown and complex due to the couple effects of magnetic saturation and core loss. Similar to the aforementioned F_{v}^0, RBF network-based data-driven method is utilized to model $\Delta F_{\mathrm{v,c}}$. As shown in Fig. 6(b), $\Delta F_{\mathrm{v,c}}$ can be represented by

$$\Delta F_{\mathrm{v,c}} = G(I_{\mathrm{s}}, \gamma, \Delta\omega) = \sum_{j=1}^{L} v_j \varphi_j \left([I_{\mathrm{s}}, \gamma, \Delta\omega]^{\mathrm{T}}\right) \tag{42}$$

with

$$\varphi_j \left([I_{\mathrm{s}}, \gamma, \Delta\omega]^{\mathrm{T}}\right) = \exp\left(-\frac{(I_{\mathrm{s}} - I_{\mathrm{s},j})^2 + (\gamma - \gamma_j)^2 + (\Delta\omega - \Delta\omega_j)^2}{2\varsigma_j^2}\right) \tag{43}$$

where v_j is the jth weight coefficient, $(I_{\mathrm{s},j}, \gamma_j, \Delta\omega_j)$ is the center of $\varphi_j(\cdot)$ and ς_j is the scale parameter that can be tuned.

Next consider the training data for obtaining the estimation of $\{I_{\mathrm{s},j}, \gamma_j, \Delta\omega_j\}_{j=1}^{L}$ and $\{v_j\}_{j=1}^{L}$. Assume that the PM temperature is maintained at T_0. For the motor speeds ω_k and ω_0, the corresponding virtual flux linkages $F_{\mathrm{v}}^k(I_{\mathrm{s},i}, \gamma_i)$ and $F_{\mathrm{v}}^0(I_{\mathrm{s},i}, \gamma_i)$ can be obtained from (13)

$$\begin{aligned} F_{\mathrm{v}}^k(I_{\mathrm{s},i},\gamma_i) &= \lambda_{\mathrm{T}}^0 \sin\gamma_i - I_{\mathrm{s},i}(L_{\mathrm{d}}\sin^2\gamma_i + L_{\mathrm{q}}\cos^2\gamma_i - L_{\mathrm{dq}}\sin 2\gamma_i) \\ &\quad + I_{\mathrm{s,c}}^{k,i}(L_{\mathrm{d}}\sin\alpha_i^k \sin\gamma_i + L_{\mathrm{q}}\cos\alpha_i^k \cos\gamma_k - L_{\mathrm{dq}}\sin(\alpha_i^k + \gamma_i)) \\ F_{\mathrm{v}}^0(I_{\mathrm{s},i},\gamma_i) &= \lambda_{\mathrm{T}}^0 \sin\gamma_i - I_{\mathrm{s},i}(L_{\mathrm{d}}\sin^2\gamma_i + L_{\mathrm{q}}\cos^2\gamma_i - L_{\mathrm{dq}}\sin 2\gamma_i) \\ &\quad + I_{\mathrm{s,c}}^{0,i}(L_{\mathrm{d}}\sin\alpha_i^0 \sin\gamma_i + L_{\mathrm{q}}\cos\alpha_i^0 \cos\gamma_i - L_{\mathrm{dq}}\sin(\alpha_i^0 + \gamma_i)). \end{aligned} \tag{44}$$

Subtracting the second equation from the first equation in (44) leads to

$$\begin{aligned} &F_{\mathrm{v}}^k(I_{\mathrm{s},i},\gamma_i) - F_{\mathrm{v}}^0(I_{\mathrm{s},i},\gamma_i) \\ &= I_{\mathrm{s,c}}^{k,i}(L_{\mathrm{d}}\sin\alpha_i^k \sin\gamma_i + L_{\mathrm{q}}\cos\alpha_i^k \cos\gamma_k - L_{\mathrm{dq}}\sin(\alpha_i^k + \gamma_i)) \\ &\quad - I_{\mathrm{s,c}}^{0,i}(L_{\mathrm{d}}\sin\alpha_i^0 \sin\gamma_i + L_{\mathrm{q}}\cos\alpha_i^0 \cos\gamma_i - L_{\mathrm{dq}}\sin(\alpha_i^0 + \gamma_i)) \\ &= \Delta F_{\mathrm{v,c}}^k(I_{\mathrm{s},i}, \gamma_i). \end{aligned} \tag{45}$$

In other words, (45) is equivalent to (18). Hence, the model of $\Delta F_{\mathrm{v,c}}^k(I_{\mathrm{s},i}, \gamma_i)$ can be built from the $F_{\mathrm{v}}^k(I_{\mathrm{s},i}, \gamma_i)$ and $F_{\mathrm{v}}^0(I_{\mathrm{s},i}, \gamma_i)$. From (12), $F_{\mathrm{v,c}}^k(I_{\mathrm{s},i}, \gamma_i)$ can be calculated by the measured voltages $V_{\mathrm{d},i}^k$ and $V_{\mathrm{q},i}^k$

$$F_{\mathrm{v,c}}^k(I_{\mathrm{s},i}, \gamma_i) = \left(V_{\mathrm{q},i}^k \sin\gamma_i + V_{\mathrm{d},i}^k \cos\gamma_i\right)/\omega_k. \tag{46}$$

Based on (45), (46), and (41), we have

$$\begin{aligned} \Delta F_{\mathrm{v,c}}^k(I_{\mathrm{s},i}, \gamma_i) = &\left(V_{\mathrm{q},i}^k \sin\gamma_k + V_{\mathrm{d},i}^k \cos\gamma_i\right)/\omega_k \\ &- \left(V_{\mathrm{q},i}^0 \sin\gamma_i + V_{\mathrm{d},i}^0 \cos\gamma_i\right)/\omega_0. \end{aligned} \tag{47}$$

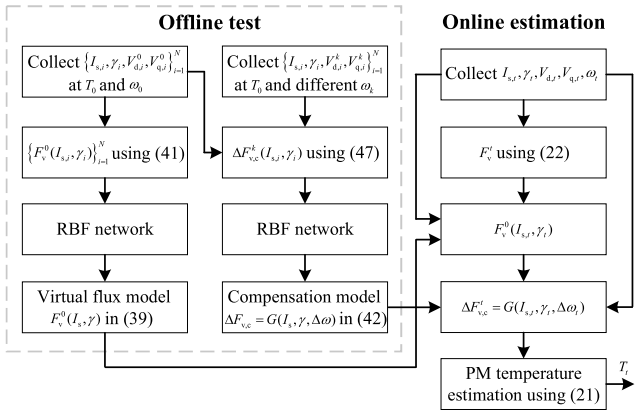

Fig. 7. Flowchart of the proposed PM temperature estimation.

Thus, $\{\Delta F_{\mathrm{v,c}}^k(I_{\mathrm{s},i}, \gamma_i)\}_{i=1}^N$ can be collected under different current conditions $\{I_{\mathrm{s},i}, \gamma_i\}_{i=1}^N$ at the speed of ω_k, and the corresponding $\Delta\omega_k = \omega_k - \omega_0$ is obtained. After data acquisition at multiple speeds $\{\omega_k\}_{k=1}^M$, the inputs $\{\{I_{\mathrm{s},i}, \gamma_i, \Delta\omega_k\}_{i=1}^N\}_{k=1}^M$ and outputs $\{\{\Delta F_{\mathrm{v,c}}^k(I_{\mathrm{s},i}, \gamma_i)\}_{i=1}^N\}_{k=1}^M$ can be constructed for RBF network training to estimate the RBF centers $\{I_{\mathrm{s},j}, \gamma_j, \Delta\omega_j\}_{j=1}^L$ and the weight coefficients $\{v_j\}_{j=1}^L$. Note that the experimental test for each speed should be conducted in a short period of time to ensure that the variation of PM temperature is negligible, and the PM temperature is kept at the room temperature T_0. This is the basis of core loss compensation modeling. The RBF network training is achieved using MATLAB neural network toolbox, in which the size of the hidden layer (L) is determined automatically based on the expected error of the network. At this point, the compensation model (42) is established.

The flowchart of the proposed PM temperature estimation is summarized in Fig. 7. An offline test is conducted to build the virtual flux model $F_{\mathrm{v}}^0(I_{\mathrm{s}}, \gamma)$ and the compensation model $\Delta F_{\mathrm{v,c}} = G(I_{\mathrm{s}}, \gamma, \Delta\omega)$ using the RBF neural networks. Further, at time t, the real-time data $I_{\mathrm{s},t}$, γ_t, $V_{\mathrm{d},t}$, $V_{\mathrm{q},t}$, and ω_t is collected to calculate the virtual flux F_{v}^t, the reference flux $F_{\mathrm{v}}^0(I_{\mathrm{s},t}, \gamma_t)$, and the core loss induced flux compensation $\Delta F_{\mathrm{v,c}}^t = G(I_{\mathrm{s},t}, \gamma_t, \Delta\omega_t)$. Then, the PM temperature T_t at time t can be estimated using (21).

IV. Experimental Investigations

The proposed approach is applied to a laboratory interior PMSM drive system, as shown in Fig. 8. The PMSM is driven by an insulated gate bipolar transistor-based inverter with the switching frequency of 10 KHz in double update mode. Moreover, it is controlled by a programmable MT1050 controller equipped with ARM Cortex-A9 CPU and 2 GB DDR3 SDRAM. The detailed machine parameters are listed in Table I. The torque/current and speed controls are adopted for the PMSM and dyno motor, respectively. Moreover, the measured PM temperature is collected by a thermal imager to evaluate the estimation accuracy of the proposed method.

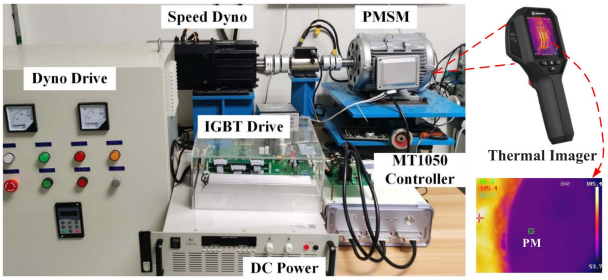

Fig. 8. Experimental setup.

TABLE I
MACHINE PARAMETERS OF THE TEST PMSM

Parameter	Value	Parameter	Value
Rated current	12 A	Winding resistance	0.25 Ω
Rated torque	20 Nm	PM flux linkage	0.25 Wb·turn
Rated speed	1000 rpm	No. of poles	8

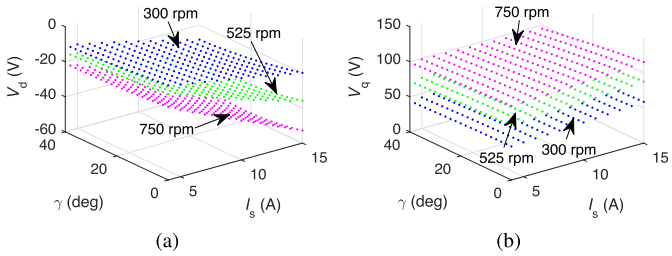

Fig. 9. Collected $\{V^0_{\mathrm{d},i}\}^N_{i=1}$ and $\{V_{\mathrm{q},0}\}^N_{i=1}$ at ω_0=300, 525, 750 rpm.

In Test 1, the data are collected for virtual flux and core loss compensation modeling. Specifically, the PMSM is operated at different speeds ($\omega_k = 300, 375, \ldots, 1050$ rpm), and for each ω_k, the voltages $V^k_{\mathrm{d},i}$ and $V^k_{\mathrm{q},i}$ at various current conditions ($I_{\mathrm{s},i} = 4, 5, \ldots, 15$ A, $\gamma_i = 0, 2, \ldots, 40°$) are collected. The test is carried out in different groups according to ω_i, and each group is completed in a short time to ensure that the change of PM temperature is negligible. It can be regarded that all data in Test 1 are collected when the PM temperature is at room temperature T_0, which is measured to be 23.9 °C. In Tests 2–4, the proposed temperature estimation method is evaluated under different operating conditions.

A. Virtual Flux and Compensation Modeling Results

The collected $\{V^0_{\mathrm{d},i}\}^N_{i=1}$ and $\{V^0_{\mathrm{q},i}\}^N_{i=1}$ under three speed conditions ($\omega_0 = 300, 525, 750$ rpm) are presented in Fig. 9. Then using (41), the training data can be calculated for establishing the virtual flux model $F^0_{\mathrm{v}}(I_{\mathrm{s}}, \gamma)$ with the RBF neural network, as shown in Fig. 10. It can be observed that for a particular current condition, the value of F^0_{v} depends on the speed. That is because the core loss varies with the speed. It is necessary to consider the core loss in PM temperature estimation for accuracy improvement, which is the motivation of this work.

For a fixed ω_0, the training data $\{\Delta F^k_{\mathrm{v,c}}(I_{\mathrm{s},i}, \gamma_i)\}^N_{i=1}$ at various ω_k can be calculated by (47), which is utilized to establish the

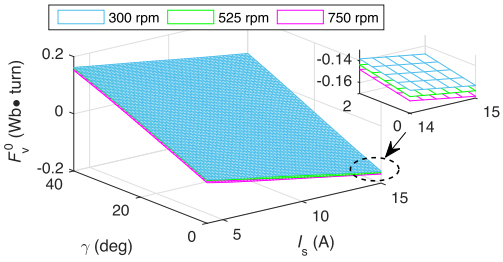

Fig. 10. Virtual flux model $F^0_{\mathrm{v}}(I_{\mathrm{s}}, \gamma)$ under three speed conditions.

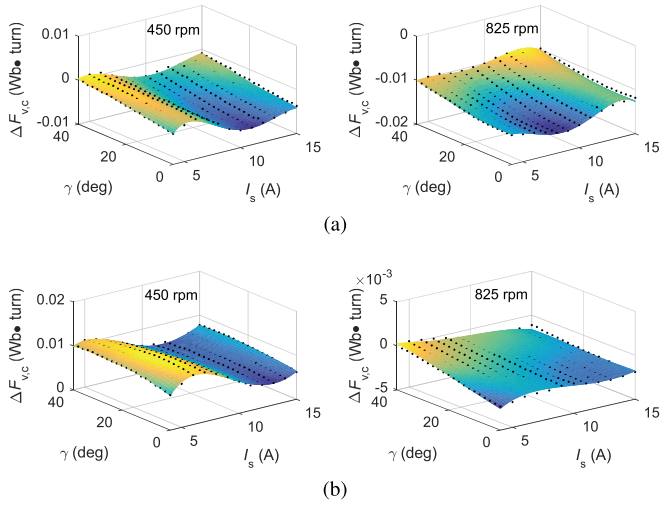

Fig. 11. Estimated core loss compensation $\Delta F_{\mathrm{v,c}}$ at the speed of 450 and 825 rpm. (a) $\omega_0 = 300$ rpm. (b) $\omega_0 = 750$ rpm.

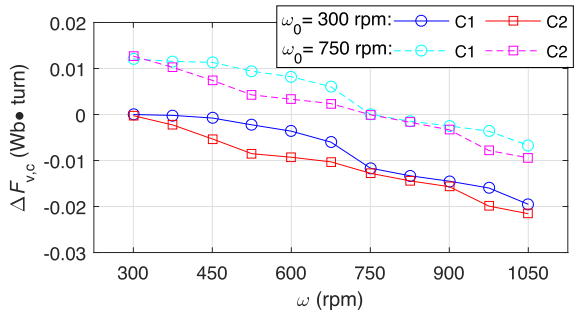

Fig. 12. Core loss compensation with respect to the speed under current conditions C1 and C2.

compensation model $\Delta F_{\mathrm{v,c}} = G(I_{\mathrm{s}}, \gamma, \Delta\omega)$. Fig. 11 shows the compensation results at the speed of 450 and 825 rpm under two reference speed conditions. As can be seen, the compensation value $\Delta F_{\mathrm{v,c}}$ varies nonlinearly with the stator current I_{s}. It implies that the core loss current $I_{\mathrm{s,c}}$ is a nonlinear function of I_{s}. Moreover, $\Delta F_{\mathrm{v,c}}$ is strongly dependent on the speed. Fig. 12 presents the compensation value with respect to the speed under two current conditions: C1 ($I_{\mathrm{s}} = 5$ A, $\gamma = 10°$) and C2 ($I_{\mathrm{s}} = 10$ A, $\gamma = 12°$). It can be observed that the amplitude of $\Delta F_{\mathrm{v,c}}$ for a certain current increases with the difference between

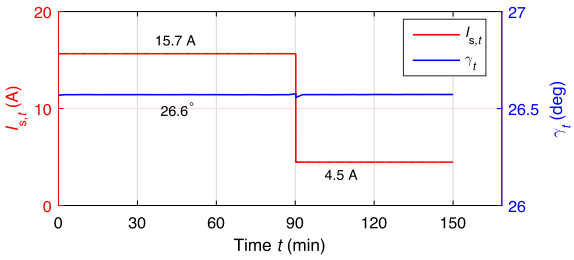

Fig. 13. Current conditions in Test 2.

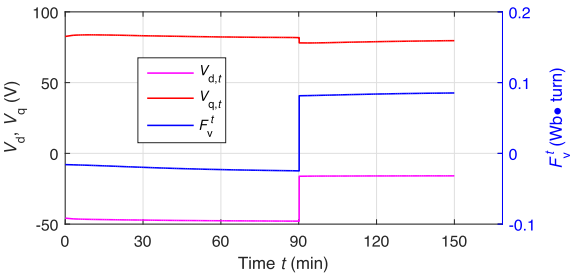

Fig. 14. Collected dq-axis voltages and calculated F_{v}^t in Test 2.

TABLE II
VIRTUAL FLUX AT DIFFERENT PM TEMPERATURES IN TEST 2

$I_{\mathrm{s},t}$ (A)	15.7			4.5		
T_t (°C)	22.0	47.1	66.4	59.0	50.5	43.4
F_{v}^t (Wb·turn)	−0.0159	−0.0210	−0.0248	0.0830	0.0845	0.0853

the speed ω and the reference one ω_0. For instance, when ω_0 is set to be 300 rpm, $\Delta F_{\mathrm{v,c}} = 0, -0.0036$ and -0.0145 Wb · turn at $\omega = 300, 600$, and 900 rpm under C1, respectively. Note that the maximum amplitude of $\Delta F_{\mathrm{v,c}}$ is more than 10% of the maximum amplitude of F_{v}^0, which means that the core loss effect is significant, especially in high-speed scenarios, and thus core loss compensation is critical.

B. PM Temperature Estimation Results

In Test 2, the motor speed $\omega_t = 600$ rpm, the current angle $\gamma_t = 26.6°$, and the current amplitude $I_{\mathrm{s},t}$ steps from 15.7 to 4.5 A at time $t = 90$ min, as presented in Fig. 13. The test lasts 150 min. The real-time dq-axis voltages $V_{\mathrm{d},t}$ and $V_{\mathrm{q},t}$ are collected to calculate the virtual flux linkage F_{v}^t. It can be seen from Fig. 14 that the values of $V_{\mathrm{d},t}$, $V_{\mathrm{q},t}$, and F_{v}^t step with the change of current at $t = 90$ min. Moreover, F_{v}^t decreases slowly at $t < 90$ min and increases at $t > 90$ min because of the change of PM temperature. Table II presents the values of F_{v}^t at different PM temperatures. It is clear that F_{v}^t varies with the stator current and the temperature, and the variation of F_{v}^t is opposite to that of temperature.

Based on the models $F_{\mathrm{v}}^0(I_{\mathrm{s}}, \gamma)$ and $\Delta F_{\mathrm{v,c}} = G(I_{\mathrm{s}}, \gamma, \Delta\omega)$ built in Test 1, $F_{\mathrm{v}}^0(I_{\mathrm{s},t}, \gamma_t)$ and the core loss compensation $\Delta F_{\mathrm{v,c}}^t = G(I_{\mathrm{s},t}, \gamma_t, \Delta\omega_t)$ under the operating condition $\{I_{\mathrm{s},t}, \gamma_t, \omega_t\}$ can be obtained. Furthermore, the PM temperature T_t can be estimated from F_{v}^t, $F_{\mathrm{v}}^0(I_{\mathrm{s},t}, \gamma_t)$ and $\Delta F_{\mathrm{v,c}}^t$ by

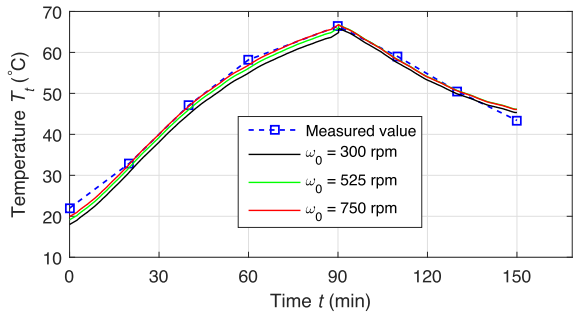

Fig. 15. Estimated and measured PM temperatures in Test 2.

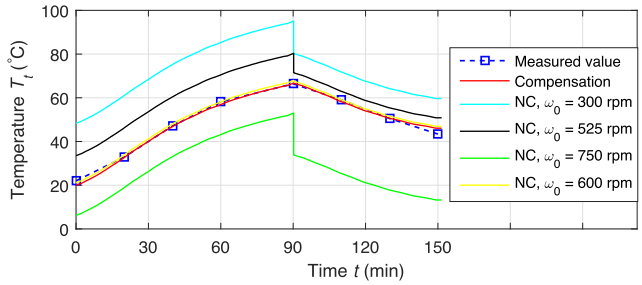

Fig. 16. Comparison of the proposed method with and without core loss compensation in Test 2. "NC" denotes the proposed method but without compensation.

using (21). The estimated results are shown in Fig. 15. It can be observed that the proposed method can provide satisfactory estimated temperatures that match the measured ones well under different reference speed (ω_0) conditions. For instance, the measured T_t is 58.2 °C at $t = 60$ min, and the estimated values using $\omega_0 = 300$, 525, and 750 rpm are 55.0 °C, 56.1 °C, and 56.9 °C with the estimation errors are 3.2 °C, 2.1 °C, and 1.3 °C, respectively. The results using $\omega_0 = 300$ rpm are slightly worse than those using $\omega_0 = 525$ and 750 rpm. The main reason is that the deviation of $\omega_t = 600$ rpm from $\omega_0 = 300$ rpm is larger than those from the other two reference speeds, and the compensation error with $\omega_0 = 300$ rpm is relatively larger. The medium speed rather than high or low speed is recommended as the reference speed to obtain better estimation results. With $\omega_0 = 750$ rpm, the estimated PM temperature first rises from 19.9 °C to 66.8 °C, and then decreases to 46.1 °C after the current step. The estimation errors are less than 3 °C, which demonstrates the effectiveness of the proposed method.

Fig. 16 presents the performance comparison of the proposed method with and without core loss compensation in Test 2. As can be seen, the proposed method with compensation performs significantly better than that without compensation in the case of $\omega_0 \neq \omega_t$. For the latter, it performs as well as the compensation method if $\omega_0 = \omega_t = 600$ rpm, since the core loss variation induced by speed is negligible. The method without compensation is sensitive to the reference speed ω_0. It is impractical to fix the real-time speed ω_t as ω_0 in industrial applications. The proposed compensation method can adapt to the core loss variation caused by the speed variation, thus leading to accurate temperature estimation. Moreover, its estimation performance

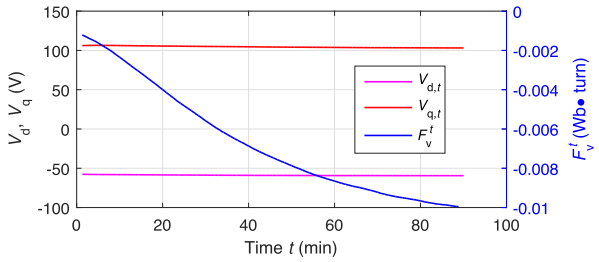

Fig. 17. Collected dq-axis voltages and calculated F_v^t in Test3.

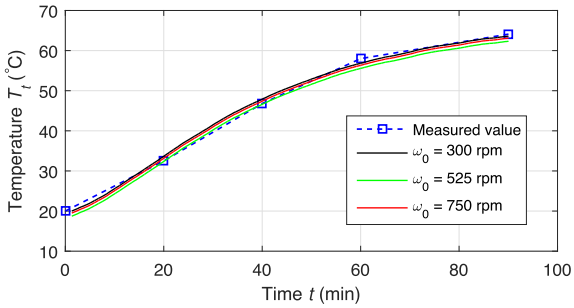

Fig. 18. Estimated and measured PM temperatures in Test3.

is independent of the selection of ω_0. If the core loss compensation is not performed, one can build the reference databases at various ω_0, and select the appropriate database according to the difference between ω_t and ω_0 in the applications. For instance, $\omega_0 = 525$ rpm is preferred in this test as compared to 300 and 750 rpm, because 525 rpm is closer to $\omega_t = 600$ rpm and the core loss variation due to the speed variation is relatively smaller. As can be seen in Fig. 16, the estimated results with $\omega_0 = 525$ rpm are better than those with 300 and 750 rpm. If the reference speed deviates significantly from the current speed, it may lead to incorrect estimation in the method without core loss compensation.

In Test 3, the motor speed $\omega_t = 825$ rpm, the current conditions are $I_{s,t} = 14.8$ A and $\gamma_t = 28.3°$. The test lasts 90 min, and the measured PM temperature rises from 20.0 °C to 64.1 °C. The collected voltages $V_{d,t}$ and $V_{q,t}$ and the calculated F_v^t are shown in Fig. 17. The value of F_v^t decreases over time due to the rise of PM temperature. Fig. 18 presents the estimated temperatures of the proposed method using different reference speeds. Compared with the measured values of 32.5 °C and 64.1 °C at $t = 40$ and 90 min, the estimation errors are 1.2 °C and 0.5 °C with $\omega_0 = 300$ rpm, 0.1 °C and 1.8 °C with $\omega_0 = 525$ rpm, 0.7 °C and 1.0 °C with $\omega_0 = 750$ rpm. The proposed method can provide accurate temperature estimation with an error of less than 2 °C. The comparative results of the proposed method with and without core loss compensation are shown in Fig. 19. It is clear that the estimated results with compensation are better than those without compensation in the case of $\omega_0 \neq \omega_t$, which further verifies the effectiveness of the proposed core loss compensation. For the method without compensation, it performs best with $\omega_0 = 825$ rpm, which is exactly the same as ω_t, following by 750, 525, and 300 rpm. In summary, the estimation accuracy of the method without compensation depends on the selection of ω_0, which affects the elimination of core loss effect

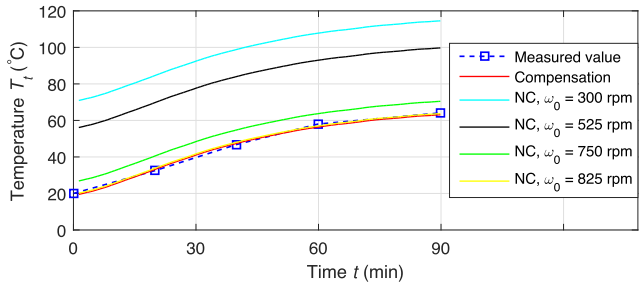

Fig. 19. Comparison of the proposed method with and without core loss compensation in Test 3. "NC" denotes the proposed method but without compensation.

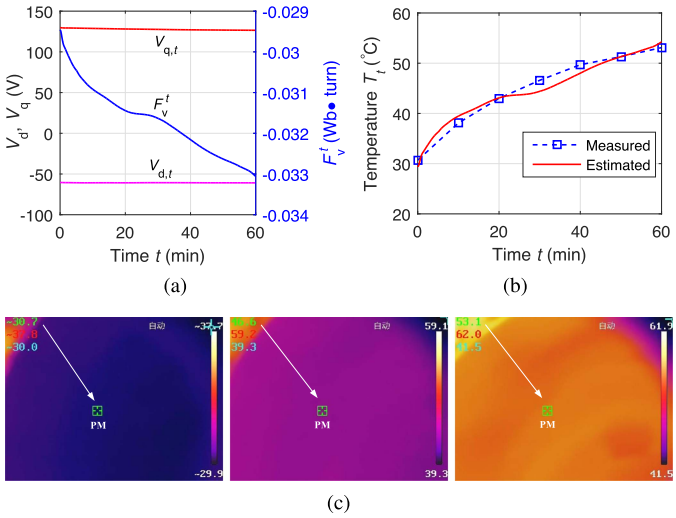

Fig. 20. Temperature estimation in the high-speed test. (a) F_v^t. (b) Comparison of the estimated and measured temperatures. (c) Thermal images of magnet at $t = 0, 30, 60$ min.

TABLE III
ESTIMATION ERROR IN THE HIGH-SPEED TEST

Time (min)	0	10	20	30	40	50	60
Measured (°C)	30.7	38.1	43.0	46.6	49.7	51.3	53.1
Estimated (°C)	29.6	39.5	43.1	44.4	48.0	51.3	54.2
Error (°C)	1.1	1.4	0.1	2.2	1.7	0.0	1.1

induced by motor speed variation. The proposed compensation method is not sensitive to ω_0, and can perform well with a fixed ω_0 through the capability of core loss compensation.

Test 4 is conducted to evaluate the proposed method under high-speed condition with large core loss. The motor speed is set to the rated value of 1000 rpm, $I_{s,t} = 12$ A, $\gamma_t = 20°$. The PM temperature is measured by the thermal imager at the interval of 10 min. Fig. 20 shows the estimation process and results of the PM temperature. As can be seen, F_v^t decreases with the temperature rise. The estimated temperatures match the measured ones well. For example, the measured temperatures are 30.7 °C and 53.1 °C at t =0 and 60 min, respectively, and the estimated values are 29.6 °C and 54.2 °C with the errors of 1.1 °C. The detailed error comparison listed in Table III shows that the maximum error is 2.2 °C. The proposed method can

TABLE IV
COMPARISON OF STATE-OF-THE-ART PM TEMPERATURE ESTIMATION METHODS

Methods	Winding resistance	Magnetic saturation	VSI nonlinearity	Core loss	Estimation accuracy	Remarks	
						Advantages	Disadvantages
LPTN [10]	√	○	○	√	$< 3.5°C$	Low risk in estimation robustness	Geometric information is required
Current injection [25]	√	√	√	×	$< 5°C$	Robust to parameter variation	Additional mechanical loss is introduced
HF voltage injection [16]	√	√	√	√	$< 3°C$	PM and winding temperatures are estimated simultaneously	Only applicable in low-speed
Reactive energy [23]	√	√	√	×	$< 3.7°C$	Inductance variation is considered	Offline test is required
Deep learning [34]	√	○	○	○	$< 5.8°C$	PM, stator teeth, winding and yoke temperatures are estimated simultaneously	High computational complexity
Proposed	√	√	√	√	$< 3°C$	Effect of resistance variation and VSI nonlinearity is cancelled, and core loss effect is modeled	Offline test is required

Note that "√", "×" and "○" represent the feature is considered, not considered and not reported yet in this article, respectively.

provide accurate temperature estimation at high speed with the capability of core loss compensation.

V. CONCLUSION

In this article, a data-driven virtual flux modeling approach with core loss compensation is proposed for PM temperature estimation. Specifically, the machine model considering the core loss and inverter nonlinearity is presented, and the virtual *dq*-axis is introduced to eliminate the effect of inverter nonlinearity and winding temperature variation. By doing so, the virtual flux linkage with core loss awareness can be constructed and expressed as a simplified linear relationship of *dq*-axis voltages. Further, the PM temperature estimation model based on virtual flux variation and core loss compensation is derived, in which the reference flux and compensation term are estimated from voltage data using the RBF neural networks. The proposed method is evaluated on a laboratory PMSM drive system under various current and speed conditions, and the estimation errors of PM temperature are less than 3 °C. The estimated temperatures with and without compensation are presented to demonstrate the contribution of core loss compensation to improving estimation accuracy.

The detailed comparison of the proposed and state-of-the-art methods is summarized in Table IV. Compared with the signal injection-based methods, the proposed method is built in the virtual reference frame, and does not introduce additional losses and noise. In addition, it is applicable to a large speed range, from low to high speeds. Compared with the LPTN-based and deep learning-based methods, the proposed method is flexible in implementation without needing of geometric information of machine or complicated calculations. It should be emphasized that an efficient way to quantify the effect of core loss on temperature estimation is also provided in the proposed method. The limitation of the proposed method is that the offline test is required to build the virtual flux model and core loss compensation model at the reference speed. However, it is computationally efficient by using the lightweight learning algorithm.

REFERENCES

[1] M. S. Rafaq and J. W. Jung, "A comprehensive review of state-of-the-art parameter estimation techniques for permanent magnet synchronous motors in wide speed range," *IEEE Trans. Ind. Inform.*, vol. 16, no. 7, pp. 4747–4758, Jul. 2020.

[2] T. Wang et al., "An EMF observer for PMSM sensorless drives adaptive to stator resistance and rotor flux linkage," *IEEE J. Emerg. Sel. Topics Power Electron.*, vol. 7, no. 3, pp. 1899–1913, Sep. 2019.

[3] S. Liu, Q. Wang, G. Zhang, G. Wang, and D. Xu, "Online temperature identification strategy for position sensorless PMSM drives with position error adaptive compensation," *IEEE Trans. Power Electron.*, vol. 37, no. 7, pp. 8502–8512, Jul. 2022.

[4] H. Jung, H. Kim, S. Sul, and D. Berry, "Magnet temperature estimation of traction motor in standstill with considering spatial harmonics," *IEEE Trans. Ind. Electron.*, vol. 68, no. 11, pp. 10546–10557, Nov. 2021.

[5] C. Lian, F. Xiao, J. Liu, and S. Gao, "Parameter and VSI nonlinearity hybrid estimation for PMSM drives based on recursive least square," *IEEE Trans. Transport. Electrific.*, vol. 9, no. 2, pp. 2195–2206, Jun. 2023.

[6] A. Balamurali, A. K. Anik, W. Clandfield, and N. C. Kar, "Non-invasive parameter and loss determination in PMSM considering the effects of saturation, cross-saturation, time harmonics, and temperature variations," *IEEE Trans. Magn.*, vol. 57, no. 2, pp. 1–6, Feb. 2021.

[7] X. Chen, J. Wang, and A. Griffo, "A high-fidelity and computationally efficient electrothermally coupled model for interior permanent-magnet machines in electric vehicle traction applications," *IEEE Trans. Transp. Electrific.*, vol. 1, no. 4, pp. 336–347, Dec. 2015.

[8] A. Tikadar, J. W. Kim, Y. Joshi, and S. Kumar, "Flow-assisted evaporative cooling for electric motor," *IEEE Trans. Transp. Electrific.*, vol. 8, no. 1, pp. 1128–1143, Mar. 2022.

[9] D. Liang et al., "Estimation of 3-D magnet temperature distribution based on lumped-parameter and analytical hybrid thermal model for SPMSM," *IEEE Trans. Energy Convers.*, vol. 37, no. 1, pp. 515–525, Mar. 2022.

[10] J. Feng, D. Liang, Z. Q. Zhu, S. Guo, Y. Li, and A. Zhao, "Improved low-order thermal model for critical temperature estimation of PMSM," *IEEE Trans. Energy Convers.*, vol. 37, no. 1, pp. 413–423, Mar. 2022.

[11] D. Reigosa, D. Fernandez, T. Tanimoto, T. Kato, and F. Briz, "Comparative analysis of BEMF and pulsating high-frequency current injection methods for PM temperature estimation in PMSMs," *IEEE Trans. Power Electron.*, vol. 32, no. 5, pp. 3691–3699, May 2017.

[12] D. D. Reigosa, D. Fernandez, H. Yoshida, T. Kato, and F. Briz, "Permanent-magnet temperature estimation in PMSMs using pulsating high-frequency current injection," *IEEE Trans. Ind. Appl.*, vol. 51, no. 4, pp. 3159–3168, Jul./Aug. 2015.

[13] D. D. Reigosa, J. M. Guerrero, A. B. Diez, and F. Briz, "Rotor temperature estimation in doubly-fed induction machines using rotating high-frequency signal injection," *IEEE Trans. Ind. Appl.*, vol. 53, no. 4, pp. 3652–3662, Jul./Aug. 2017.

[14] G. Feng, C. Lai, and N. C. Kar, "Expectation-maximization particle-filter- and Kalman-filter-based permanent magnet temperature estimation for pmsm condition monitoring using high-frequency signal injection," *IEEE Trans. Ind. Inform.*, vol. 13, no. 3, pp. 1261–1270, Jun. 2017.

[15] Y.-C. Kwon, J. Lee, and S.-K. Sul, "Recent advances in sensorless drive of interior permanent-magnet motor based on pulsating signal injection," *IEEE J. Emerg. Sel. Topics Power Electron.*, vol. 9, no. 6, pp. 6577–6588, Dec. 2021.
[16] H. Kim, H. Jung, and S. Sul, "Stator winding temperature and magnet temperature estimation of IPMSM based on high-frequency voltage signal injection," *IEEE Trans. Ind. Electron.*, vol. 70, no. 3, pp. 2296–2306, Mar. 2023.
[17] H.-S. Jung, D. Park, H. Kim, S.-K. Sul, and D. J. Berry, "Non-invasive magnet temperature estimation of IPMSM based on high-frequency inductance with a pulsating high-frequency voltage signal injection," *IEEE Trans. Ind. Appl.*, vol. 55, no. 3, pp. 3076–3086, May/Jun. 2019.
[18] D. Reigosa, D. Fernandez, M. Martinez, J. M. Guerrero, A. B. Diez, and F. Briz, "Magnet temperature estimation in permanent magnet synchronous machines using the high frequency inductance," *IEEE Trans. Ind. Appl.*, vol. 55, no. 3, pp. 2750–2757, May/Jun. 2019.
[19] G. Feng, C. Lai, and N. C. Kar, "Speed harmonic based modeling and estimation of permanent magnet temperature for PMSM drive using Kalman filter," *IEEE Trans. Ind. Inform.*, vol. 15, no. 3, pp. 1372–1382, Mar. 2019.
[20] S. Xiao and A. Griffo, "PWM-based flux linkage and rotor temperature estimations for permanent magnet synchronous machines," *IEEE Trans. Power Electron.*, vol. 35, no. 6, pp. 6061–6069, Jun. 2020.
[21] N. Z. Popov, S. N. Vukosavic, and E. Levi, "Motor temperature monitoring based on impedance estimation at PWM frequencies," *IEEE Trans. Energy Convers.*, vol. 29, no. 1, pp. 215–223, Mar. 2014.
[22] K. Yu, Z. Wang, X. Wang, and Z. Zou, "An online flux estimation for dual three-phase SPMSM drives using position-offset injection," *IEEE Trans. Power Electron.*, vol. 36, no. 10, pp. 11606–11617, Oct. 2021.
[23] H.-S. Jung, H. Kim, S.-K. Sul, and D. J. Berry, "Temperature estimation of IPMSM by using fundamental reactive energy considering variation of inductances," *IEEE Trans. Power Electron.*, vol. 36, no. 5, pp. 5771–5783, May 2021.
[24] K. Liu and Z. Zhu, "Position-offset-based parameter estimation using the adaline NN for condition monitoring of permanent-magnet synchronous machines," *IEEE Trans. Ind. Electron.*, vol. 62, no. 4, pp. 2372–2383, Apr. 2015.
[25] G. Feng, C. Lai, W. Li, Z. Li, and N. C. Kar, "Efficient permanent magnet temperature modeling and estimation for dual three-phase PMSM considering inverter nonlinearity," *IEEE Trans. Power Electron.*, vol. 35, no. 7, pp. 7328–7340, Jul. 2020.
[26] P. Kakosimos and H. Abu-Rub, "Deadbeat predictive control for PMSM drives with 3-L NPC inverter accounting for saturation effects," *IEEE J. Emerg. Sel. Topics Power Electron.*, vol. 6, no. 4, pp. 1671–1680, Dec. 2018.
[27] M. Taherzadeh, M. A. Hamida, M. Ghanes, and M. Koteich, "A new torque observation technique for a PMSM considering unknown magnetic conditions," *IEEE Trans. Ind. Electron.*, vol. 68, no. 3, pp. 1961–1971, Mar. 2021.
[28] G. Feng, C. Lai, X. Tan, W. Peng, and N. C. Kar, "Multi-parameter estimation of PMSM using differential model with core loss compensation," *IEEE Trans. Transp. Electrific.*, vol. 8, no. 1, pp. 1105–1115, Mar. 2022.
[29] C. Desai and P. Pillay, "Back EMF, torquecangle, and core loss characterization of a variable-flux permanent-magnet machine," *IEEE Trans. Transp. Electrific.*, vol. 5, no. 2, pp. 371–384, Jun. 2019.
[30] N. Boubaker, D. Matt, P. Enrici, F. Nierlich, and G. Durand, "Measurements of iron loss in PMSM stator cores based on CoFe and SiFe lamination sheets and stemmed from different manufacturing processes," *IEEE Trans. Magn.*, vol. 55, no. 1, pp. 1–9, Jan. 2019.
[31] Z. Jin, J. Yang, X. Qiu, H. Ge, and C. Bai, "A high torque estimation accuracy direct torque control of permanent magnet synchronous motor based on a novel iron loss resistance observer," *IEEE Access*, vol. 9, pp. 125822–125829, 2021.
[32] H. Zhang, M. Dou, and C. Dang, "Loss-optimization method of permanent-magnet synchronous motor based on precise stator iron loss model," *IEEE J. Emerg. Sel. Topics Power Electron.*, vol. 9, no. 5, pp. 5407–5415, Oct. 2021.
[33] A. Balamurali, G. Feng, C. Lai, J. Tjong, and N. C. Kar, "Maximum efficiency control of PMSM drives considering system losses using gradient descent algorithm based on DC power measurement," *IEEE Trans. Energy Convers.*, vol. 33, no. 4, pp. 2240–2249, Dec. 2018.
[34] W. Kirchgassner, O. Wallscheid, and J. Bocker, "Estimating electric motor temperatures with deep residual machine learning," *IEEE Trans. Power Electron.*, vol. 36, no. 7, pp. 7480–7488, Jul. 2021.
[35] S. Li, B. Sarlioglu, S. Jurkovic, N. R. Patel, and P. Savagian, "Comparative analysis of torque compensation control algorithms of interior permanent magnet machines for automotive applications considering the effects of temperature variation," *IEEE Trans. Transp. Electrific.*, vol. 3, no. 3, pp. 668–681, Sep. 2017.
[36] B.-H. Bae and S.-K. Sul, "A compensation method for time delay of full-digital synchronous frame current regulator of PWM AC drives," *IEEE Trans. Ind. Appl.*, vol. 39, no. 3, pp. 802–810, May/Jun. 2003.
[37] A. G. Yepes, A. Vidal, J. Malvar, O. Lpez, and J. Doval-Gandoy, "Tuning method aimed at optimized settling time and overshoot for synchronous proportional-integral current control in electric machines," *IEEE Trans. Power Electron.*, vol. 29, no. 6, pp. 3041–3054, Jun. 2014.

Kaide Huang received the B.S. and Ph.D. degrees in engineering from Sun Yat-sen University, Guangzhou, China, in 2011 and 2016, respectively.

He is currently an Associate Professor with the School of Mathematics and Big Data, Foshan University, Foshan, China. From 2017 to 2018, he was an Assistant Chief Engineer with Computer Network Information Center, Chinese Academy of Sciences, Guangzhou, China. His research interests include artificial intelligence algorithm and electrical machine optimization control.

Beichen Ding (Member, IEEE) received the Ph.D. degree in mechanical engineering from the University of Bath, Bath, U.K., in 2019.

He is currently an Associate Professor with the School of Advanced Manufacturing, Sun Yat-sen University, Guangzhou, China. His research interests include actuation and motion control of smart machine systems, and adaptive control for nonlinear systems.

Chunyan Lai (Senior Member, IEEE) received the B.S. degree in engineering from Sun Yat-sen University, Guangzhou, China, in 2010, and the Ph.D. degree in electrical and computer engineering from the University of Windsor, Windsor, ON, Canada, in 2017.

She is currently an Associated Professor with the Department of Electrical and Computer Engineering, Concordia University, Montreal, QC, Canada. From 2017 to 2018, she was as a Postdoctoral Fellow with the University of Windsor. Her research interests include electric machine drives and controls, and other power electronics related applications, such as renewable energy.

Dr. Lai is an Associate Editor for IEEE SYSTEMS JOURNAL.

Guodong Feng (Senior Member, IEEE) received the B.S. and Ph.D. degrees in engineering from Sun Yat-sen University, Guangzhou, China, in 2010 and 2015, respectively.

He is currently an Associate Professor with the School of Intelligent Systems Engineering, Sun Yat-sen University. From 2015 to 2019, he was a Postdoctoral Fellow with the University of Windsor, Windsor, ON, Canada. His research interests include advanced signal processing, optimization, and electrical machines and drives.

Dr. Feng is an Associate Editor for IEEE TRANSACTIONS ON INDUSTRIAL ELECTRONICS.